Numerical simulation of thermal behavior of lithium-ion secondary batteries using the enhanced single particle model

Naoki Baba [a,*], Hiroaki Yoshida [a], Makoto Nagaoka [a], Chikaaki Okuda [b], Shigehiro Kawauchi [b]

[a] *Thermodynamic System Research Div., Toyota Central R&D Labs., Inc., Nagakute, Aichi 480-1192, Japan*
[b] *Energy Creation & Storage Div., Toyota Central R&D Labs., Inc., Nagakute, Aichi 480-1192, Japan*

HIGHLIGHTS

- We propose an enhanced single particle (ESP) model for lithium-ion batteries.
- The ESP model accounts for the solution phase limitation.
- The ESP model is available for the high rate charge–discharge analysis.
- We report the two-way electrochemical-thermal coupled simulation method.
- Temperature estimates during the charge–discharge cycle are calculated accurately.

ARTICLE INFO

ABSTRACT

To understand the thermal behavior of lithium-ion secondary batteries, distributed information related to local heat generation across the entire electrode plane, which is caused by the electrochemical reaction that results from lithium-ion intercalation or deintercalation, is required. To accomplish this, we first developed an enhanced single particle (ESP) model for lithium-ion batteries that provides a cost effective, timely, and accurate method for estimating the local heat generation rates without excessive computation costs. This model accounts for all the physical processes, including the solution phase limitation. Next, a two-way electrochemical-thermal coupled simulation method was established. In this method, the three dimensional (3D) thermal solver is coupled with the quasi-3D porous electrode solver that is applied to the unrolled plane of spirally wound electrodes, which allows both thermal and electrochemical behaviors to be reproduced simultaneously at every computational time-step. The quasi-3D porous electrode solver implements the ESP model.

This two-way coupled simulation method was applied to a thermal behavior analysis of 18650-type lithium-ion cells where it was found that temperature estimates of the electrode interior and on the cell can wall obtained via the ESP model were in good agreement with actual experimental measurements.

© 2013 Elsevier B.V. All rights reserved.

1. Introduction

Lithium-ion batteries are attractive power sources for hybrid electric vehicles (HEVs) and electric vehicles (EVs) because they offer high cell voltages and energy densities. As a result, significant amounts of research have been focused on improving the power density, energy density, and life cycle performance of such batteries. However, because one of the primary issues in designing

lithium-ion batteries is ensuring safety, ceaseless efforts have been expended towards overcoming thermal stability problems.

When evaluating thermal stability in the battery design phase, numerical simulation techniques provide useful information that is difficult or impossible to obtain experimentally. As a result, there have been numerous previous reports on thermal modeling of lithium-ion batteries over a wide range of exposed conditions. Many such reports go beyond normal use [1–11], with some focusing specifically on thermal abuse [12,13].

For example, Pals and Newman performed one-dimensional (1D) thermal modeling experiments to calculate temperature profiles in cell stacks [5,6]. This work was based on the 1D macroscopic model developed by Doyle and Newman [14] with the addition of a

lumped heat generation term presented by Bernardi et al. [15] Chen and Evans [7–9] presented a multi-dimensional thermal model for lithium-ion batteries that focused on heat transport inside the cell stack without considering the electrochemistry of the cell. In their work, the heat generation rate was estimated using experimental discharged curves based on the lumped heat generation formulas given by Bernardi et al. Kim et al. [10,11] applied a two-dimensional (2D) model to parallel plate battery electrodes in order to simulate not only the potential and current density distribution, but also the temperature distribution. However, their modeling approach focused on ensuring current continuity on the electrodes and lumped heat generation terms in a fashion similar to the above-mentioned models.

In this study, we focus on the thermal behaviors of lithium-ion batteries under normal operating conditions. The objective of our work is the development of a multi-dimensional simulation method capable of evaluating both electrochemical and thermal behaviors inside lithium-ion batteries as accurately as possible, without the use of a lumped heat generation formula.

In order to achieve this, it was first necessary to develop a new variation of the commonly used single particle (SP) model for lithium-ion batteries. The previous simplified battery model [16–21] neglects the solution phase limitation. In contrast, the new and simplified battery model presented in this paper is capable of estimating heat generation rates using a detailed theoretical formula [1–3], since it accounts for all the physical processes, including the solution phase limitation.

Subsequently, a quasi-3D porous electrode solver was developed implementing the above new simplified battery model. This solver is basically applied to the 2D unrolled plane of spirally wound electrodes and provides distributed information on the potentials and lithium-ion concentrations, not only across the entire 2D electrode plane, but also across the thickness of the electrode itself, which can be obtained with the assistance of the new simplified battery model. As a result, the local heat generation rate resulting from the electrochemical reactions that occur during the charge–discharge process can be calculated in accordance with the detailed theoretical formula, and its 2D distribution data can be obtained across the entire electrode plane.

Finally, a two-way electrochemical-thermal coupled simulation method has also been established. Rising temperatures in a lithium-ion battery affect its performance because both the transport and physical properties strongly depend on temperature. In this method, the quasi-3D porous electrode solver transfers the information of the planer distribution of the heat generation rate to the 3D thermal solver. Following that, the 3D thermal solver simulates the temperature distribution of the spirally wound electrodes and returns the temperature information to the quasi-3D porous electrode solver. By executing the above-mentioned data exchange process, the temperature dependency of the transport and physical properties can be considered at every computational time-step.

This paper describes the abovementioned new charge–discharge SP model for lithium-ion batteries and the two-way electrochemical-thermal coupled simulation method in detail. In Sections 2 and 3, model development and validation of the new simplified battery model are shown in comparison with the conventional SP model. In Section 4, the two-way electrochemical-thermal coupled simulation method is described. In Section 6, simulated results of the electrochemical and thermal behaviors of a 18650-type lithium-ion cell during the charge–discharge cycle are expressed and discussed in detail with the aid of temperature measurements obtained from inside a real cell, which is shown in Section 5. Finally, conclusions of this paper are presented in Section 7.

2. Model development

In this section, the modeling approach for our new charge–discharge SP model for lithium-ion batteries is described in detail.

2.1. Conventional lithium-ion battery models

The literature on modeling approaches for lithium-ion batteries is quite extensive. However, conventional mathematical models can be classified roughly into two categories.

The first modeling approach was proposed by Doyle and Newman [14]. A schematic of this model, which consists of two composite electrodes and a separator, is shown in Fig. 1 and is referred to as the Newman model hereafter. A mathematical representation includes equations that describe: (1) mass transport of lithium in the solid phases, (2) mass transport of lithium-ions in the solution phase, (3) charge transport in the solid phases, and (4) charge transport in the solution phase. The Newman model is treated as a 1D macroscopic model across the thickness of the electrode in the local point on the electrode plane. To put it more precisely, the concentration of lithium within the solid phase is solved rigorously, using the extra pseudo second dimension along the radius of the particle. From the viewpoint of application to the 3D electrochemical-thermal coupled simulation for lithium-ion batteries, the advantage of the Newman model is its ability to accurately estimate heat generation rates, whereas its demerit is its high computational costs. The local heat generation rate is calculated from the detailed theoretical formula shown below [1–3].

$$q = \sigma^{\text{eff}} \nabla \phi_s \cdot \nabla \phi_s + \left(\kappa^{\text{eff}} \nabla \phi_e \cdot \nabla \phi_e + \kappa_D^{\text{eff}} \nabla \ln c_e \cdot \nabla \phi_e \right) + a_{s,j} \bar{i}_{n,j} (\phi_s - \phi_e - U_j) + a_{s,j} \bar{i}_{n,j} T \frac{\partial U_j}{\partial T}$$

(1)

Eq. (1) requires the local point values and gradients of potentials and concentrations in the solid and electrolyte phase. Since the Newman model can be used to estimate these values at the each local point, the heat generation rate can be accurately estimated via Eq. (1). On the other hand, the Newman model requires the use of a μm-order mesh size to discretize a calculation domain across the thickness of each electrode in 1D. As a result, if the entire lithium-ion cell geometry of a 18650-type cell is discretized with the μm-order size, the number of computational meshes will be far in excess of ten million, which makes this methodology expensive and time consuming.
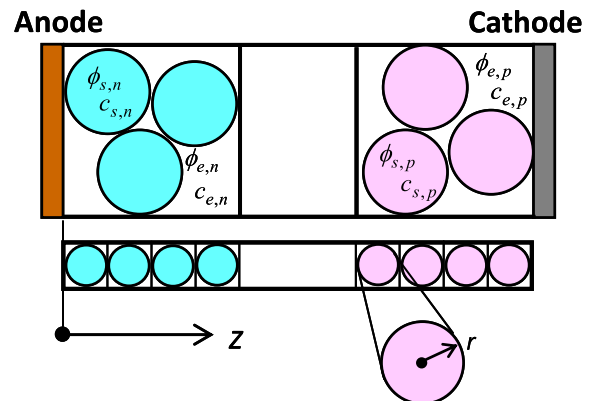

Fig. 1. Schematic of the lithium-ion battery model proposed by Doyle and Newman [12].

The second modeling approach is the SP model [16–21]. A schematic of this model is shown in Fig. 2. In this model, each electrode is represented by a single spherical particle. When considering the 3D electrochemical-thermal coupled simulation of lithium-ion batteries, it is important to reflect on the advantages and drawbacks of the SP model. The advantages of the SP model include its simplicity and reduced computation time requirements. This model is orders of magnitude faster than the Newman model. However, a significant drawback of the SP model is that it assumes that the electrolyte phase diffusion limitations are ignored. Hence, potentials in the electrolyte phase are set to zero, and concentrations in the electrolyte phase are set to a constant value. This renders estimations of the heat generation rate via Eq. (1) inadequate. Furthermore, even if the heat generation rate is estimated using the lumped formula presented by Bernardi et al. [15], the resulting estimated values seem to have less accuracy.

2.2. Description of new SP model

In the above discussion, the advantages and drawbacks of conventional lithium-ion battery models were classified. In the present paper, from the viewpoint of application to the 3D electrochemical-thermal coupled simulation, we propose a new lumped model for lithium-ion batteries.

This model combines advantages of both the Newman and SP models. However, to be successful, the new lumped model must provide the following advantages:

(a) Calculation costs equivalent to that of the SP model
(b) Heat release rate estimation accuracy at same level as the Newman model

The development concept of a new lumped model is based on the SP model with specific consideration paid to the electrolyte phase diffusion limitations. Fig. 3 shows a schematic of a new lumped model, which is referred to hereafter as the enhanced single particle (ESP) model. In the ESP model, each electrode is represented by a single spherical particle along with its electrolyte phase. The potential and lithium concentration in the solid phase are calculated in the same way as with the conventional SP model. Additionally, the potential and lithium-ion concentration in the electrolyte phase are set at the representative position in the each electrode.

The most important advancement over the SP model at this point is that these physical quantities are approximated by parabolic profiles within each electrode. As described in Eq. (1), accurate heat release rate estimates require the point values and gradients of these physical quantities. These point values and gradients are calculated from approximated parabolic profiles, which makes it possible for the ESP model to calculate the heat release rate. Furthermore, the potentials and lithium-ion concentrations at interfaces between the negative and the separator, or between the positive and the separator, are implicitly considered in the ESP
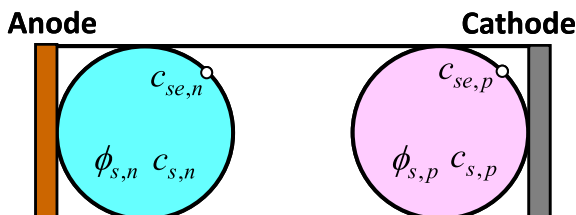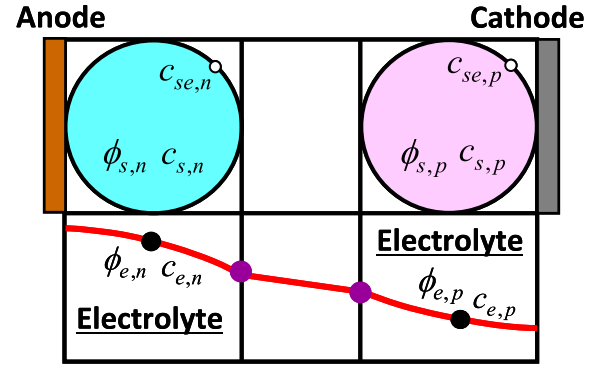

Fig. 3. Schematic of the ESP model. In this model, each of negative and positive electrodes is represented by a single spherical particle in the electrolyte phase.

model. Mass transport and charge transport between both electrodes in the electrolyte phase, which satisfies the mass and charge conservation, are estimated using these boundary values.

2.3. Model equations

2.3.1. Calculation procedure of concentrations

Fig. 4 describes the procedure for calculating ESP model concentrations in detail.

Fick's second law usually describes the lithium transport in the solid phase, with the following boundary conditions set for a spherical particle:

$$\frac{\partial c_s}{\partial t} = D_s \left[\frac{\partial^2 c_s}{\partial r^2} + \frac{2}{r} \frac{\partial c_s}{\partial r} \right] \tag{2}$$

$$-D_s \frac{\partial c_s}{\partial r} = 0 \quad \text{at } r = 0 \tag{3}$$

$$-D_s \frac{\partial c_s}{\partial r} = \frac{\bar{i}_n}{F} \quad \text{at } r = r_s \tag{4}$$

In the conventional SP model, the diffusion length method [22] is introduced to simplify the diffusion equation. By assuming a parabolic concentration profile in the diffusion layer and using the
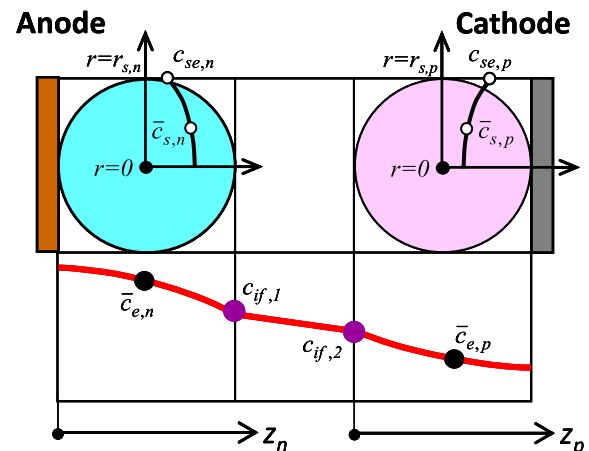

Fig. 2. Schematic of the single particle (SP) model. This model assumes that the electrolyte phase diffusion limitations are ignored.

Fig. 4. Calculation procedure of the concentration field of the ESP model.

volume average technique, the solutions for Eqs. (2)–(4) can be approximated with a set of differential and algebraic equations:

$$\frac{d\bar{c}_{s,j}}{dt} + \frac{15D_{s,j}}{r_{s,j}^2}\left(\bar{c}_{s,j} - c_{se,j}\right) = 0 \tag{5}$$

$$-D_{s,j}\frac{\left(c_{se,j} - \bar{c}_{s,j}\right)}{l_{se,j}} = \frac{j_j^{Li}}{a_{s,j}F} \tag{6}$$

where $l_{se,j}$ is the diffusion length and takes the value of $r_{s,j}/5$ for spherical particles. In view of the need to reduce computational costs, the diffusion length method is implemented to the ESP model in the same way.

The diffusion limitations in the electrolyte phase are also considered in the ESP model. The representative lithium-ion concentrations of electrolyte in each electrode region are defined by using the volume average technique as follows:

$$\bar{c}_{e,n} = \frac{1}{L_n}\int_0^{L_n} c_{e,n}dz_n \tag{7}$$

$$\bar{c}_{e,p} = \frac{1}{L_p}\int_0^{L_p} c_{e,p}dz_p \tag{8}$$

In the ESP model, a parabolic concentration profile is assumed in each region. Therefore, the positions corresponding to the representative concentrations are

$$z_{n,e}^* = \frac{1}{\sqrt{3}}\cdot L_n \tag{9}$$

$$z_{p,e}^* = \left(1 - \frac{1}{\sqrt{3}}\right)\cdot L_p \tag{10}$$

where the extra pseudo coordinates z_n and z_p are defined as shown in Fig. 4.

In addition, as Fig. 4 also shows, the concentrations on the negative/separator interface and the separator/positive interface are implicitly defined as $c_{if,1}$ and $c_{if,2}$, respectively. The interfacial balances of lithium-ion flux yield are

$$-D_{e,n}^{eff}\frac{c_{if,1} - \bar{c}_{e,n}}{\delta_n} = -D_{e,sep}^{eff}\frac{c_{if,2} - c_{if,1}}{L_{sep}} \tag{11}$$

$$-D_{e,sep}^{eff}\frac{c_{if,2} - c_{if,1}}{L_{sep}} = -D_{e,p}^{eff}\frac{\bar{c}_{e,p} - c_{if,2}}{\delta_p} \tag{12}$$

where δ_n and δ_p represent the diffusion length in each region which are expressed as [22]

$$\delta_n = \frac{L_n}{3} \quad \text{and} \quad \delta_p = \frac{L_p}{3} \tag{13}$$

Solving Eqs. (11) and (12) gives the interfacial concentrations as

$$c_{if,1} = \frac{\alpha_n + \omega}{\alpha_n + \omega + \gamma_p}\cdot\bar{c}_{e,n} + \frac{\gamma_p}{\alpha_n + \omega + \gamma_p}\cdot\bar{c}_{e,p} \tag{14}$$

$$c_{if,2} = \frac{\alpha_n}{\alpha_n + \omega + \gamma_p}\cdot\bar{c}_{e,n} + \frac{\omega + \gamma_p}{\alpha_n + \omega + \gamma_p}\cdot\bar{c}_{e,p} \tag{15}$$
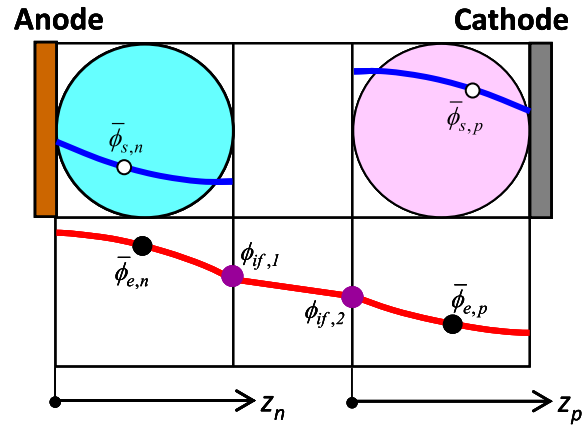

Fig. 5. Calculation procedure of the potential field of the ESP model.

$$\alpha_n = \frac{D_{e,n}^{eff}}{\delta_n}, \quad \beta_{sep} = \frac{D_{e,sep}^{eff}}{L_{sep}}, \quad \gamma_p = \frac{D_{e,p}^{eff}}{\delta_p} \quad \text{and} \quad \omega = \frac{\gamma_p\cdot\alpha_n}{\beta_{sep}} \tag{16}$$

The equations for calculating the time evolution of the volume averaged lithium-ion concentration in the electrolyte phase are derived as shown below. As for the negative, conservation of lithium-ion [14] in the electrolyte yields

$$\varepsilon_{e,n}\frac{\partial c_{e,n}}{\partial t} = D_{e,n}^{eff}\frac{\partial^2 c_{e,n}}{\partial z_n^2} + \frac{1 - t_+^\circ}{F}j_n^{Li} \tag{17}$$

As shown in Fig. 4, the electrolyte phase concentration is represented by a parabolic profile:

$$c_{e,n} = a\cdot z_n^2 + b\cdot z_n + c \tag{18}$$

where the three coefficients, a, b and c can be determined by the following boundary conditions and Eq. (7).

$$\frac{\partial c_{e,n}}{\partial z_n} = 0 \quad \text{at} \quad z_n = 0 \tag{19}$$

$$c_{e,n} = c_{if,1} \quad \text{at} \quad z_n = L_n \tag{20}$$

Application of volume averaging to Eq. (17) and substitution of Eq. (18) results in

$$\varepsilon_{e,n}\frac{d\bar{c}_{e,n}}{dt} = D_{e,n}^{eff}\cdot(2a) + \frac{1 - t_+^\circ}{F}j_n^{Li} \tag{21}$$

Substituting the coefficient a into Eq. (21) yields

$$\varepsilon_{e,n}\frac{d\bar{c}_{e,n}}{dt} = A_n\cdot\bar{c}_{e,n} + B_n\cdot\bar{c}_{e,p} + \frac{1 - t_+^\circ}{F}j_n^{Li} \tag{22}$$

where the coefficients A_n and B_n are given by

$$A_n = -\frac{1}{L_n}\cdot\frac{\gamma_p\cdot\alpha_n}{\alpha_n + \omega + \gamma_p} \tag{23}$$

$$B_n = \frac{1}{L_n}\cdot\frac{\gamma_p\cdot\alpha_n}{\alpha_n + \omega + \gamma_p} \tag{24}$$

As for the positive, the same procedure mentioned above also yields the equation for calculating the time evolution of the volume averaged lithium-ion concentration in the electrolyte phase:

$$\varepsilon_{e, p} \frac{d\bar{c}_{e, p}}{dt} = A_p \cdot \bar{c}_{e, n} + B_p \cdot \bar{c}_{e, p} + \frac{1 - t_+^\circ}{F} j_p^{Li} \qquad (25)$$

where the coefficients A_p and B_p are given by

$$A_p = \frac{1}{L_p} \cdot \frac{\gamma_p \cdot \alpha_n}{\alpha_n + \omega + \gamma_p} \qquad (26)$$

$$B_p = -\frac{1}{L_p} \cdot \frac{\gamma_p \cdot \alpha_n}{\alpha_n + \omega + \gamma_p} \qquad (27)$$

Currently, in the ESP model, Eqs. (5), (6), (22) and (25) are specified in order to solve the mass transport of the system.

2.3.2. Calculation procedure of potentials

With the assistance of Fig. 5, the calculation procedure of potentials of the ESP model is described in detail. In analogy with the calculation procedure of concentrations, the potentials on the negative/separator interface and the separator/positive interface are implicitly defined as $\phi_{if, 1}$ and $\phi_{if, 2}$, respectively.

The boundary conditions for the solid phase potential $\phi_{s,n}$ in the negative electrode are described below. On the copper current collector/composite negative electrode interface, $\phi_{s,n}$ is arbitrarily set to zero, while on the same interface, the solid phase current density is equated to the applied current density, namely

$$\phi_{s, n} = 0 \quad \text{at} \quad z_n = 0 \qquad (28)$$

$$-\sigma_n^{eff} \frac{\partial \phi_{s, n}}{\partial z_n} = I_{app} \quad \text{at} \quad z_n = 0 \qquad (29)$$

On the negative/separator interface, the charge flux in the solid phase is equated to zero.

$$\frac{\partial \phi_{s, n}}{\partial z_n} = 0 \quad \text{at} \quad z_n = L_n \qquad (30)$$

Applying a parabolic profile for $\phi_{s,n}$, satisfaction of the above boundary conditions results in

$$\phi_{s, n} = \frac{1}{2L_n} \cdot \frac{I_{app}}{\sigma_n^{eff}} \cdot z_n^2 - \frac{I_{app}}{\sigma_n^{eff}} \cdot z_n \qquad (31)$$

The representative potential in the negative solid phase is defined by using the volume average technique.

$$\bar{\phi}_{s, n} = \frac{1}{L_n} \int_0^{L_n} \phi_{s, n} dz_n \qquad (32)$$

Substituting Eq. (31) into Eq. (32) gives

$$\bar{\phi}_{s, n} = -\frac{1}{3} \cdot \frac{L_n}{\sigma_n^{eff}} \cdot I_{app} \qquad (33)$$

This is equal to the point value that is calculated in the profile, Eq. (31), at

$$z_{n, s}^* = \left(1 - \frac{1}{\sqrt{3}}\right) \cdot L_n \qquad (34)$$

The calculation procedure of the other potentials ($\bar{\phi}_{e, n}$, $\phi_{if, 1}$, $\phi_{if, 2}$, $\bar{\phi}_{e, p}$, $\bar{\phi}_{s, p}$) are described sequentially below.

Because Eq. (33) gives the solid phase potential, $\bar{\phi}_{s, n}$, the representative potential in the negative electrolyte region, $\bar{\phi}_{e, n}$, is determined by the following Butler–Volmer equation, namely

$$\frac{I_{app}}{L_n} = a_{s, n} i_{0, n} \left[\exp\left(\frac{\alpha_{a, n} F}{RT} \eta_n\right) - \exp\left(-\frac{\alpha_{c, n} F}{RT} \eta_n\right)\right] \qquad (35)$$

where the surface overpotential, η_n, is defined to be

$$\eta_n = \bar{\phi}_{s, n} - \bar{\phi}_{e, n} - U_n - \bar{i}_{n, n} \cdot R_{f, n} \qquad (36)$$

Conservation of charge in the electrolyte phase results in [14]

$$\nabla \cdot \left(\kappa_j^{eff} \nabla \phi_{e, j}\right) + \nabla \cdot \left(\kappa_{D, j}^{eff} \nabla \ln c_{e, j}\right) + j_j^{Li} = 0 \qquad (37)$$

From Eq. (37), the charge flux on the negative/separator interface is equated to the applied current density:

$$-\kappa_n^{eff} \frac{\partial \phi_{e, n}}{\partial z_n}\bigg|_{z_n = L_n} - \kappa_{D, n}^{eff} \frac{\frac{\partial c_{e, n}}{\partial z_n}\big|_{z_n = L_n}}{c_{if, 1}} = I_{app} \qquad (38)$$

Since the second term of the left-hand side is estimated using Eqs. (14) and (18), the potential gradient on the negative/separator interface (the first term) is obtained from Eq. (38). Next, a parabolic profile is assumed for the electrolyte potential across the thickness of the negative electrode. This parabolic profile must meet the following three conditions:

$$\frac{\partial \phi_{e, n}}{\partial z_n} = \quad \text{at} \quad z_n = 0 \qquad (39)$$

$$\frac{\partial \phi_{e, n}}{\partial z_n} = s_{if, 1} \quad \text{at} \quad z_n = L_n \qquad (40)$$

$$\bar{\phi}_{e, n} = \frac{1}{L_n} \int_0^{L_n} \phi_{e, n} dz_n \qquad (41)$$

where $s_{if, 1}$ is the electrolyte potential gradient on the negative/separator interface, which is estimated from Eq. (38). Using Eqs. (39)–(41), the potential profile in the negative electrolyte region is found to be determined by

$$\phi_{e, n} = \frac{s_{if, 1}}{2L_n} \cdot z_n^2 + \bar{\phi}_{e, n} - \frac{s_{if, 1}}{6} \cdot L_n \qquad (42)$$

According to Eq. (42), the interfacial potential $\phi_{if, 1}$ is readily found to be expressed by

$$\phi_{if, 1} = \frac{s_{if, 1}}{3} \cdot L_n + \bar{\phi}_{e, n} \qquad (43)$$

Taking into account the continuity of the charge flux in the electrolyte phase, the charge transport in the separator leads to

$$\phi_{if, 2} = \phi_{if, 1} - \frac{1}{\kappa_{sep}^{eff}} \left(I_{app} \cdot L_{sep} + \kappa_{D, sep}^{eff} \cdot \ln \frac{c_{if, 2}}{c_{if, 1}}\right) \qquad (44)$$

where the interfacial concentrations, $c_{if, 1}$ and $c_{if, 2}$, can be estimated by Eqs. (14) and (15).

A similar calculation procedure, which is mentioned above, derives the parabolic profile for the positive electrolyte potential. The charge flux on the positive/separator interface is equated to the applied current density:

$$-\kappa_p^{eff} \frac{\partial \phi_{e, p}}{\partial z_p}\bigg|_{z_p = 0} - \kappa_{D, p}^{eff} \frac{\frac{\partial c_{e, p}}{\partial z_p}\big|_{z_p = 0}}{c_{if, 2}} = I_{app} \qquad (45)$$

The second term on the left is estimated by using Eq. (15) and the parabolic profile of $c_{e, p}$. This allows the potential gradient on

the separator/positive interface in the first term to be estimated. A parabolic profile is assumed for the electrolyte potential across the thickness of the positive electrode. This parabolic profile must satisfy the following conditions:

$$\phi_{e,p} = \phi_{if,2} \quad \text{at} \quad z_p = 0 \tag{46}$$

$$\frac{\partial \phi_{e,p}}{\partial z_p} = s_{if,2} \quad \text{at} \quad z_p = 0 \tag{47}$$

$$\frac{\partial \phi_{e,p}}{\partial z_p} = 0 \quad \text{at} \quad z_p = L_p \tag{48}$$

where $s_{if,2}$ is the electrolyte potential gradient on the separator/positive interface, which is estimated from Eq. (45). Using Eqs. (46)–(48), the potential profile in the positive electrolyte phase is found to be expressed by

$$\phi_{e,p} = -\frac{s_{if,2}}{2L_p} \cdot z_p^2 + s_{if,2} \cdot z_p + \phi_{if,2} \tag{49}$$

The representative potential in the positive electrolyte is defined to be

$$\overline{\phi}_{e,p} = \frac{1}{L_p} \int_0^{L_p} \phi_{e,p} dz_p = \frac{s_{if,2}}{3} L_p + \phi_{if,2} \tag{50}$$

This is equal to the point value that is calculated in the profile of Eq. (49) at $z_{p,e}^*$ (Eq. (10)).

Finally, let us turn to the positive solid phase potential. As Eq. (50) gives the electrolyte phase potential, the representative potential in the positive solid phase, $\overline{\phi}_{s,p}$, is estimated by the following Butler–Volmer equation, namely

$$-\frac{I_{app}}{L_p} = a_{s,p} i_{0,p} \left[\exp\left(\frac{\alpha_{a,p} F}{RT} \eta_p\right) - \exp\left(-\frac{\alpha_{c,p} F}{RT} \eta_p\right) \right] \tag{51}$$

where the surface overpotential, η_p, is defined to be

$$\eta_p = \overline{\phi}_{s,p} - \overline{\phi}_{e,p} - U_p - \overline{i}_{n,p} \cdot R_{f,p} \tag{52}$$

Just as in the case of the solid phase potential in the negative electrode, $\phi_{s,n}$, a parabolic profile is assumed and must meet the following conditions to determine the three coefficients.

$$\frac{\partial \phi_{s,p}}{\partial z_p} = 0 \quad \text{at} \quad z_p = 0 \tag{53}$$

$$-\sigma_{s,p}^{\text{eff}} \frac{\partial \phi_{s,p}}{\partial z_p} = I_{app} \quad \text{at} \quad z_p = L_p \tag{54}$$

$$\overline{\phi}_{s,p} = \frac{1}{L_p} \int_0^{L_p} \phi_{s,p} dz_p \tag{55}$$

Satisfaction of above conditions results in

$$\phi_{s,p} = -\frac{1}{2L_p} \cdot \frac{I_{app}}{\sigma_{s,p}^{\text{eff}}} \cdot z_p^2 + \frac{L_p}{6} \cdot \frac{I_{app}}{\sigma_{s,p}^{\text{eff}}} + \overline{\phi}_{s,p} \tag{56}$$

The representative value, $\overline{\phi}_{s,p}$, is obtained in the profile, Eq. (56), at

$$z_{p,s}^* = \frac{1}{\sqrt{3}} \cdot L_p \tag{57}$$

2.3.3. Summary of model equations

Model equations of the ESP model are now specified completely. The final equations are summarized in Table 1. Time evolutions of unknowns are calculated by using the set of equations for volume averaging values.

Here, the relationship between the conventional SP model and the ESP model is worth a passing mention. The conventional SP model assumes that the diffusion limitations in the electrolyte phase are negligible. This assumption leads to omitting all equations in the electrolyte phase from the ESP model presented in this paper. The conservation of charge in the negative solid phase is given by

$$\sigma_n^{\text{eff}} \frac{\partial^2 \phi_{s,n}}{\partial z_n^2} - j_n^{\text{Li}} = 0 \tag{58}$$

Applying Eq. (31) to Eq. (58) yields

$$\frac{I_{app}}{L_n} - j_n^{\text{Li}} = 0 \tag{59}$$

The above equation is also used in the conventional SP model. Note that the ESP model that neglects the electrolyte phase diffusion limitations reduces to the conventional SP model.

2.3.4. Estimation of heat generation rate

The heat generation rate during the charge–discharge process, which is Eq. (1) as revised for the ESP model, is expressed by

$$\begin{aligned} q = &\sum_{j=n,p} \left(\sigma_j^{\text{eff}} \nabla \phi_{s,j} \cdot \nabla \phi_{s,j} \right) + \sum_{j=n,\text{sep},p} \left(\kappa_j^{\text{eff}} \nabla \phi_{e,j} \cdot \nabla \phi_{e,j} \right. \\ &\left. + \kappa_{D,j}^{\text{eff}} \nabla \ln c_{e,j} \cdot \nabla \phi_{e,j} \right) + \sum_{j=n,p} a_{s,j} \overline{i}_{n,j} \left(\overline{\phi}_{s,j} - \overline{\phi}_{e,j} - U_j \right) \\ &+ \sum_{j=n,p} a_{s,j} \overline{i}_{n,j} T \frac{\partial U_j}{\partial T} \end{aligned} \tag{60}$$

The first term results from the ohmic heat in the solid phase, while the second term arises from the ohmic heat in the electrolyte phase. The summation of the last two terms accounts for irreversible and reversible heats associated with charge transfer at the solid/electrolyte interfaces. The third term represents the potential deviation from the equilibrium potential (irreversible heat). The fourth term arises from the entropic effect (reversible heat).

From Eq. (60), it is clear that the estimation of ohmic heats in the solid and electrolyte phases needs the information about the gradients of the unknowns. The ESP model includes the profile information of concentrations and potentials across the thickness of the electrode as standard features, as shown in Table 1. The gradients of concentrations and potentials in the solid phase are estimated in each parabolic profile at the positions of $z_{n,s}^*$ (Eq. (34), for the negative) and $z_{p,s}^*$ (Eq. (57), for the positive). Additionally, the gradients in the electrolyte phase are estimated in each parabolic profile at the positions of $z_{n,e}^*$ (Eq. (9), for the negative) and $z_{p,e}^*$ (Eq. (10), for the positive). As for estimation of irreversible and reversible heats, volume averaging values are used.

3. Model validation

3.1. Comparison with Newman model accuracy

First we examined the cell potential during galvanostatic discharge at various current densities for the cell described in Ref. 23. This cell consists of a carbon negative electrode (Li_xC_6), a

Table 1
Summary of model equations.

	Variable	Equation	Profile in the electrode
Species concentration in solid phase	$\overline{c}_{s,j} \quad j = n, p$	$\frac{\partial \overline{c}_{s,j}}{\partial t} + \frac{15 D_{s,j}}{r_{s,j}^2}(\overline{c}_{s,j} - c_{se,j}) = 0$	
	$\overline{c}_{se,j} \quad j = n, p$	$-D_{s,j}\frac{(c_{se,j} - \overline{c}_{s,j})}{l_{se,j}} = \frac{j_j^{Li}}{a_{s,j}F}$	
Species concentration in electrolyte phase	$\overline{c}_{e,j} \quad j = n, p$	$\varepsilon_{e,j}\frac{\partial \overline{c}_{e,j}}{\partial t} = A_j \cdot \overline{c}_{e,n} + B_j \cdot \overline{c}_{e,p} + \frac{1-t_+^c}{F}j_j^{Li}$	$c_{e,n} = \frac{3}{2L_n^2}(c_{if,1} - \overline{c}_{e,n})\cdot z_n^2 - \frac{1}{2}(c_{if,1} - 3\overline{c}_{e,n})$
			$c_{e,p} = \frac{3}{2L_p^2}(c_{if,2} - \overline{c}_{e,p})\cdot z_n^2 - \frac{3}{L_p}(c_{if,2} - \overline{c}_{e,p})\cdot z_n + c_{if,2}$
Solid phase potential	$\overline{\phi}_{s,n}$	$\overline{\phi}_{s,n} = -\frac{1}{3}\cdot\frac{L_n}{\sigma_n^{eff}}\cdot I_{app}$	$\phi_{s,n} = \frac{1}{2L_n}\cdot\frac{I_{app}}{\sigma_n^{eff}}\cdot z_n^2 - \frac{I_{app}}{\sigma_n^{eff}}\cdot z_n$
	$\overline{\phi}_{s,p}$	$-\frac{I_{app}}{L_p} = a_{s,p}i_{0,p}\left[\exp\left(\frac{\alpha_{a,p}F}{RT}\eta_p\right) - \exp\left(-\frac{\alpha_{c,p}F}{RT}\eta_p\right)\right]$	$\phi_{s,p} = -\frac{1}{2L_p}\cdot\frac{I_{app}}{\sigma_{s,p}^{eff}}\cdot z_p^2 + \frac{L_p}{6}\cdot\frac{I_{app}}{\sigma_{s,p}^{eff}} + \overline{\phi}_{s,p}$
		$\eta_p = \overline{\phi}_{s,p} - \overline{\phi}_{e,p} - U_p - \overline{i}_{n,p}\cdot R_{f,p}$	
Electrolyte phase potential	$\overline{\phi}_{e,n}$	$\frac{I_{app}}{L_n} = a_{s,n}i_{0,n}\left[\exp\left(\frac{\alpha_{a,n}F}{RT}\eta_n\right) - \exp\left(-\frac{\alpha_{c,n}F}{RT}\eta_n\right)\right]$	$\phi_{e,n} = \frac{s_{if,1}}{2L_n}\cdot z_n^2 + \overline{\phi}_{e,n} - \frac{s_{if,1}}{6}\cdot L_n$
		$\eta_n = \overline{\phi}_{s,n} - \overline{\phi}_{e,n} - U_n - \overline{i}_{n,n}\cdot R_{f,n}$	
	$\overline{\phi}_{e,p}$	$\overline{\phi}_{e,p} = \frac{s_{if,2}}{3}L_p + \phi_{if,2}$	$\phi_{e,p} = -\frac{s_{if,2}}{2L_p}\cdot z_p^2 + s_{if,2}\cdot z_p + \phi_{if,2}$

manganese oxide positive electrode ($Li_yMn_2O_4$) and a plasticized electrolyte. The solution used in the cell is 2 M $LiPF_6$ in a 1:2 ratio mixture of EC/DMC in the plasticized polymer matrix. The 1C rate of discharge is 1.75 mA cm^{-2}. For the values of the parameters used in the simulations, see Ref. [23].

Fig. 6 shows a comparison of simulated discharge curves between the Newman and conventional SP models. In Fig. 6, the cell potential is given as a function of the capacity (mAh cm^{-2}) for discharges at various rates. As pointed out in Ref. [17], the conventional SP model is as valid as the Newman model for discharge rates up to 1C. However, the slight discrepancy from the Newman model observed even at the 0.5C rate should not be overlooked. As stated in Section 2.1, the conventional SP model assumes the concentration and potential in the electrolyte phase to be constant throughout the discharge. Even at low discharge rates, the concentration change in the electrolyte phase arises moderately. The conventional SP model completely ignores this change, while the Newman model follows it via electrolyte phase charge/species conservation equations. This is reflected in the above slight discrepancy. As observed from the figure, the difference between the two models becomes increasingly large at rates of discharge beyond 1C. This suggests that the concentration and potential gradients in the electrolyte phase limit calculation accuracy under these conditions.

On the other hand, validation of the ESP model presented in this paper is clearly displayed in Fig. 7. It is important to note that a significantly good degree of agreement is observed between the

discharge curves of both the Newman and ESP models for rates up to 2C. The ESP model is capable of capturing the time variations of concentration and potential in the solution phase during the discharge process through the use of the equations shown in Table 1. This advantage over the conventional SP model leads to a good degree of agreement. At the 3C or 4C rate, the discharge curve of the ESP model is calculated below the result of Newman model in the early discharge stages, in contrast with the results of the conventional SP model shown in Fig. 6. As a result, the following additional efforts have been made to reduce this ESP model error.

As with the conventional SP model, the ESP model employs the diffusion length method inside a spherical particle with a second-degree polynomial (Eqs. (5) and (6)). The method, in itself, should be valid only after the diffusion layer builds up to its steady state. Therefore, under very high rates of discharge, the approximation that fixes the diffusion length at a constant steady state value from the beginning of the discharge is inadequate [20,24]. In view of the method shortcoming mentioned above, the time-variant diffusion length was proposed by Wang and Srinivasan [24]:

$$l_{se,j}(t) = l_{se,j}^*\left(1 - \exp\left(-\chi_{s,j}\cdot\frac{\sqrt{D_{s,j}\cdot t}}{l_{se,j}^*}\right)\right) \qquad (61)$$

where $l_{se,j}^*$ takes the value of $r_{s,j}/5$ for spherical particles, and $\chi_{s,j}$ is the tuning parameter. The empirical term was formed based on the observation that the surface concentration increases exponentially
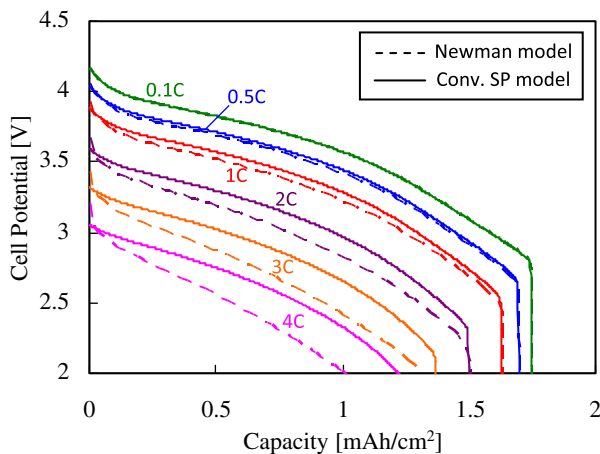

Fig. 6. Comparison between discharge curves at various rates from the Newman model and those predicted by the conventional SP model.
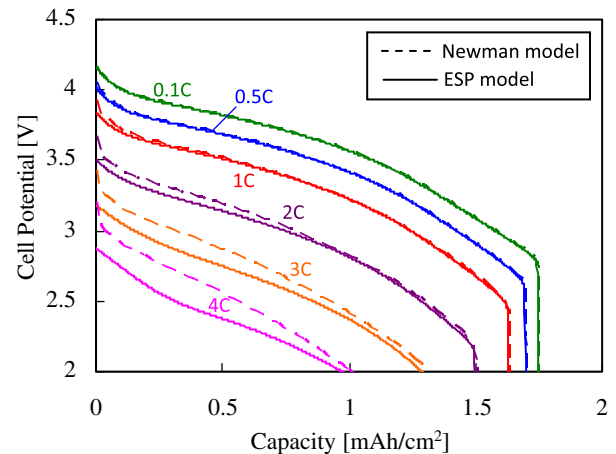

Fig. 7. Comparison between discharge curves at various rates from the Newman model and those predicted by the enhanced SP model (ESP model).
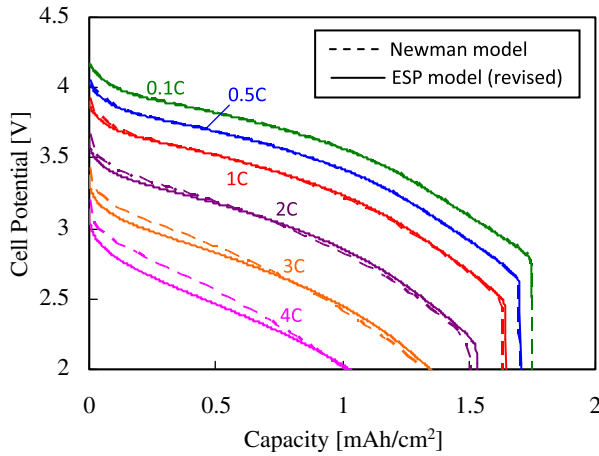
Fig. 8. Comparison between discharge curves at various rates from the Newman model and those predicted by the revised ESP model.

at short times. Furthermore, the ESP model also employs the diffusion length method concerning the electrolyte phase diffusion. The diffusion length is represented by Eq. (13). Based on the similar discussion as in the case of the solid phase diffusion, the time-variant diffusion length is introduced to the ESP model.

$$\delta_j(t) = \delta_j^* \left(1 - \exp \left(-\chi_{e,j} \cdot \frac{\sqrt{D_{e,j} \cdot t}}{\delta_j^*} \right) \right) \quad (62)$$

Here, δ_j^* is given by Eq. (13), and χ_{ej} is the tuning parameter.

Fig. 8 shows a comparison between the simulated discharge curves of the Newman and revised ESP models using Eqs. (61) and (62). These simulation results clearly indicate that the revised ESP model can provide results that are as accurate as the Newman model, even at high discharge rates.

3.2. Experimental verification

In this section, experimental verification of the ESP model is described. The comparison of the simulated discharge curves for the 18650-type lithium-ion cell is shown in Fig. 9. This cell was
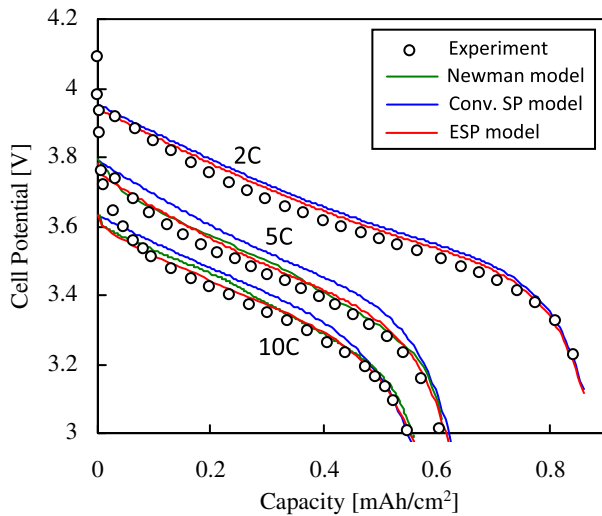

Fig. 9. Experimental validation of the ESP model. This figure compares simulated discharged curves of the 18650-type lithium-ion cell (in-house manufactured) at various rates. The lines denote model predictions while circles denote the experimental data.
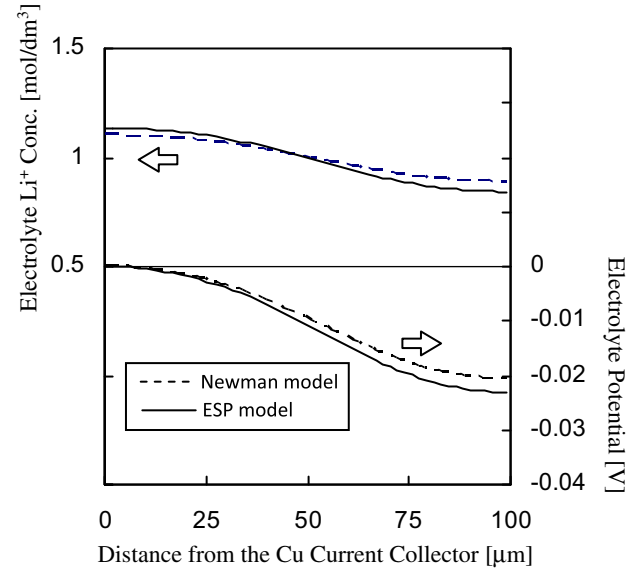

Fig. 10. Validation of the predicted profiles in the electrolyte phase concentration and potential across the thickness of the electrode at DOD = 30% during the 5C discharge rate (in-house manufactured 18650-type lithium-ion cell). The solid lines denote model predictions by the ESP model while the dashed lines denote the Newman model predictions.

manufactured in-house and consists of a carbon negative electrode, a Ni-based oxide positive electrode and a separator. The capacity of the cell is approximately 0.5 Ah. As observed at a 2C discharge rate, both the conventional SP and ESP models show good agreement with the experimental discharge curve. However, there is a significant difference between simulated results under very high discharge rates. At the 5C and 10C discharge rates, both the Newman and ESP models show good degrees of agreement with the experimental discharge curves. More specifically, the ESP model is able to provide predictions that are as accurate as the Newman model. On the other hand, the simulated discharge curves obtained via the conventional SP model show a significant discrepancy beyond the experimental results, which denote the same tendency observed in Fig. 6.

Incidentally, the ESP model provides the profile information for concentrations and potentials across the thickness of the electrode, as shown in Table 1. Fig. 10 shows a comparison of the concentration and potential profiles in the electrolyte phase across the thickness of the electrode when the depth of discharge (DOD) equals 30% during the 5C discharge rate. This figure shows that concentration and potential profiles across the thickness can be simulated by the ESP model as accurately as by Newman model.

Finally, let's summarize the advantages of the ESP model presented in this paper.

(a) The ESP model is based on the same mass-point system used by the conventional lumped model. Therefore, this model is inexpensive in terms of cost and computation time, and is thus suitable for the sub-model that is integrated into 3D simulation code.
(b) The ESP model provides profile information on concentrations and potentials across the thickness of the electrode. This enables heat generation rate estimations that are as accurate as the Newman model.

These two advantages are essential for achieving a multi-dimensional electrochemical-thermal coupled simulation required for lithium-ion batteries.
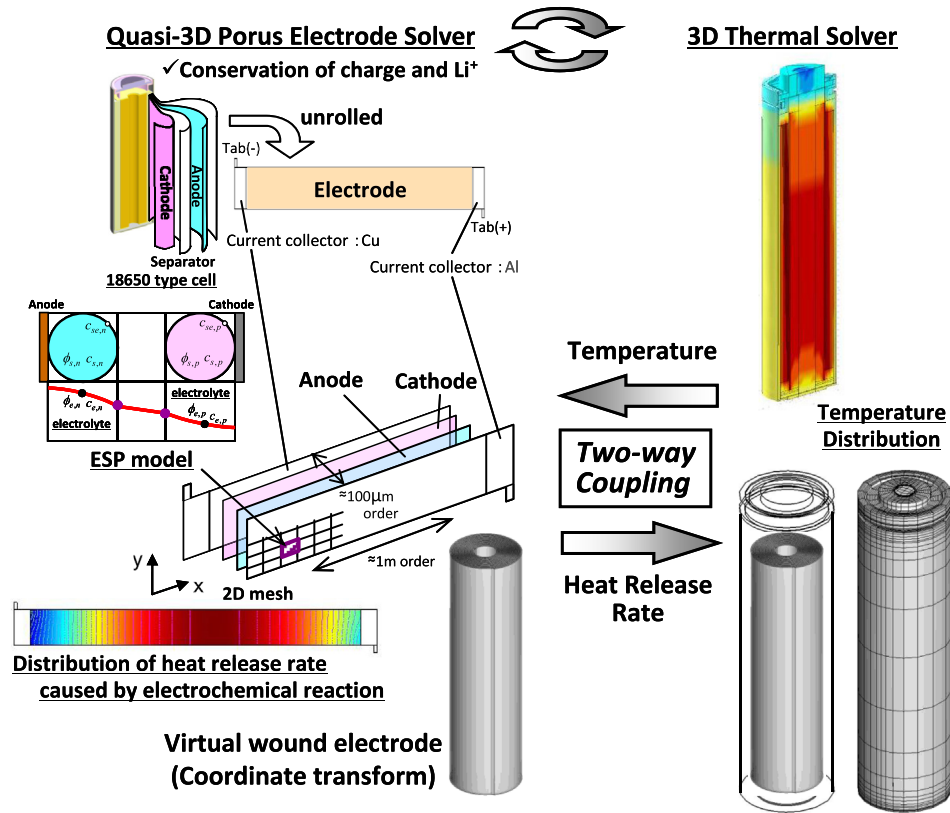
Fig. 11. A schematic of the two-way electrochemical-thermal coupled simulation method of lithium-ion batteries.

4. Two-way coupling analysis

4.1. Numerical procedure

In our approach, the electrochemical and thermal behaviors of lithium-ion batteries are simulated using two separate in-house codes. Fig. 11 shows a schematic of our two-way electrochemical-thermal coupled simulation method for lithium-ion batteries.

The quasi-3D porous electrode solver is applied for the 2D unrolled plane of the spirally wound electrodes. Usually, since the curvature radius of a spirally wound object is sufficiently large (in relation to the thickness of the electrode of a positive/negative pole) even if it treats the electrochemical reaction between electrodes at the plane locally, the potential for error is small and 2D deployment approximation is possible. Thus, the ESP model could be implemented into each 2D mesh. Conservation equations of charge and lithium-ion are solved in the 2D domain by estimating their transport across the electrode thickness using the ESP model. In this meaning, we call this code the quasi-3D solver. Then, potential and lithium-ion distributions across the 2D unrolled electrode plane are produced. From these results, we can obtain the distribution of the heat generation rate, which is estimated by Eq. (60).

Next, a virtual spirally wound electrode is constructed by the coordinate transform of the unrolled electrode plane with keeping the heat generation rate distribution information. Following this, estimated heat generation rate data are mapped to the 3D domain of the real electrode region, which is used in the 3D thermal solver, and the 3D distribution of the mapped heat generation rate q_{mapped} is reconstructed. This mapping procedure is carried out by means of the code coupling interface (CCI) [25], which is supplied by AVL List GmbH and which makes it easy for both codes to exchange the specific data.

Overviews of the 3D thermal solver and the coordinate transform in the data mapping procedure are presented in Appendix A.

The 3D thermal solver simulates the temperature distribution of the real cell using the mapped heat release rate arising from the electrochemical reaction. Next, the 3D mesh of the spirally wound electrode region in the real cell geometry is virtually unrolled onto the 2D electrode plane by the reverse coordinate transform. Following this, temperature data are mapped to the 2D unrolled electrode plane by means of CCI.

The abovementioned two-way data exchange process between two separate solvers is performed at every computational time-step; as a result, both electrochemical and thermal behaviors can
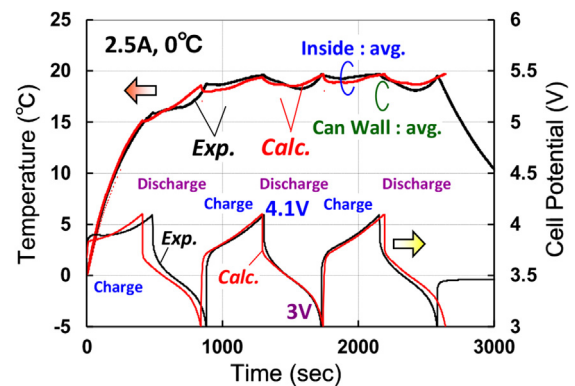

Fig. 12. Comparison between time evolutions of temperatures for the 18650-type lithium-ion cell obtained from experiment and those predicted by the two-way coupled simulation method. The time evolutions of cell potential during the charge–discharge cycle are also shown in this figure. Applied current is 2.5 A (5C), and ambient temperature is 0 °C.

be reproduced simultaneously. Additionally, physical properties are updated depending on the temperature at every computational time-step.

4.2. Implementation of ESP model

In this section, the formulation necessary to implement the ESP model into the quasi-3D porous electrode solver is described in detail.

As mentioned above, the ESP model is implemented into each 2D mesh of the unrolled electrode plane. However, a set of spirally wound electrodes consists of current collectors, composite negative and positive electrodes, and a separator. Hence, an actual unrolled electrode plane is usually in the order of 100 μm thick. Accordingly, the electrochemical analysis of unrolled electrodes should be strictly performed in 3D-mesh with an extremely large aspect ratio L/D (L: electrode length, D: electrode thickness).

For example, the 3D governing equation of charge conservation in the negative electrolyte phase is given by

$$
\kappa_n^{\text{eff}} \left(\frac{\partial^2 \phi_{e,n}}{\partial x^2} + \frac{\partial^2 \phi_{e,n}}{\partial y^2} + \frac{\partial^2 \phi_{e,n}}{\partial z^2} \right) + \kappa_{D,n}^{\text{eff}} \left(\frac{\partial^2 \ln c_{e,n}}{\partial x^2} + \frac{\partial^2 \ln c_{e,n}}{\partial y^2} \right. \\
\left. + \frac{\partial^2 \ln c_{e,n}}{\partial z^2} \right) + j_n^{\text{Li}} = 0
$$

(63)

where a x−y plane is the unrolled electrode plane. In the quasi-3D porous electrode solver, Eq. (63) reduces to the 2D equation with the additional source term as follows:

$$
\kappa_n^{\text{eff}} \left(\frac{\partial^2 \phi_{e,n}}{\partial x^2} + \frac{\partial^2 \phi_{e,n}}{\partial y^2} \right) + \kappa_{D,n}^{\text{eff}} \left(\frac{\partial^2 \ln c_{e,n}}{\partial x^2} + \frac{\partial^2 \ln c_{e,n}}{\partial y^2} \right) \\
+ j_n^{\text{Li}} - \frac{i_{\text{sepa}}}{L_n} = 0
$$

(64)

The last term on the left-hand side represents the charge transfer from the anode to the cathode via the separator, and can be formulated using the ESP model as follows:
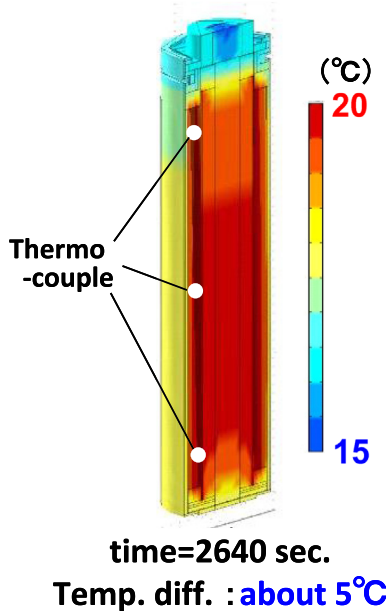

Thermo-couple

time=2640 sec.
Temp. diff. : about 5°C

Fig. 13. Simulated temperature distribution inside the cell at the end of charge–discharge cycle. Applied current is 2.5 A (5C), and ambient temperature is 0 °C.

Fig. 14. Comparison between time evolutions of temperatures for the 18650-type lithium-ion cell from experiment and those predicted by the two-way coupled simulation method. The time evolutions of cell potential during the charge−discharge cycle are also shown in this figure. Applied current is 2.5 A (5C), and ambient temperature is 20 °C.

$$
i_{\text{sepa}} = -\kappa_n^{\text{eff}} \frac{\partial \phi_{e,n}}{\partial z} \bigg|_{z=L_n} - \kappa_{D,n}^{\text{eff}} \frac{\partial \ln c_{e,n}}{\partial z} \bigg|_{z=L_n} \\
= -\kappa_n^{\text{eff}} \frac{3}{L_n} \left(\phi_1 - \overline{\phi}_{e,n} \right) - \kappa_{D,n}^{\text{eff}} \frac{\frac{3}{L_n} (c_1 - \overline{c}_{e,n})}{c_1}
$$

(65)

Other 3D governing equations for charge and lithium-ion transfer can be formulated in an analogous manner.

5. Temperature measurement

In order to evaluate the calculation accuracy of the two-way electrochemical-thermal coupled simulation method presented in this paper, temperatures inside the cell had to be measured. For this purpose, we used an in-house manufactured 18650-type lithium-ion cell with a capacity of 0.5 Ah. The cell consists of Ni-based

time=4130 sec.
Temp. diff. : about 4°C

Fig. 15. Simulated temperature distribution inside the cell at the end of charge–discharge cycle. Applied current is 2.5 A (5C), and ambient temperature is 20 °C.
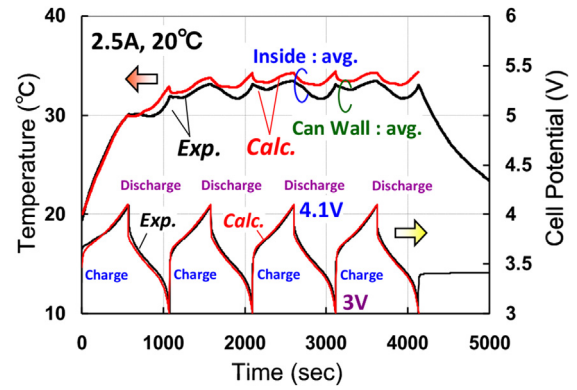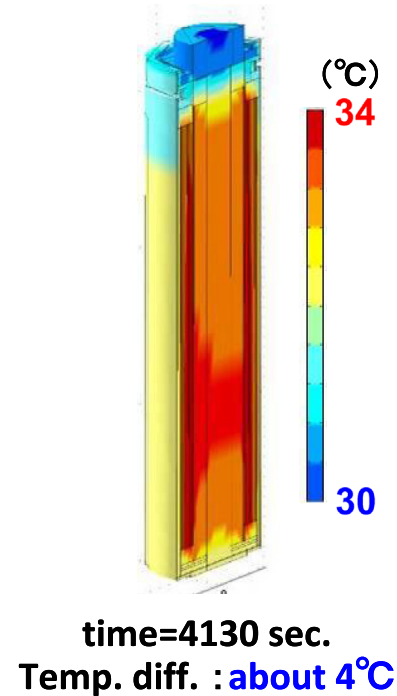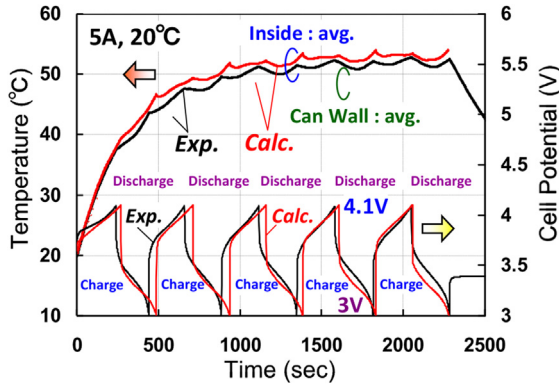
Fig. 16. Comparison between time evolutions of temperatures for the 18650-type lithium-ion cell from experiment and those predicted by the two-way coupled simulation method. The time evolutions of cell potential during the charge–discharge cycle are also shown in this figure. Applied current is 5 A (10C), and ambient temperature is 20 °C.

composite oxides positive and graphite negative. Experimental conditions were set as follows. Ambient temperatures are 0 and 20 °C. The charge–discharge condition is Constant Current (CC) with no rest. Applied currents are 2.5 and 5.0 A. Cut-off voltages are 4.1 V for charge and 3.0 V for discharge.

Two 18650-type lithium-ion cells were supplied for measurement purposes, while type-T (copper-constantan) thermocouples were used for the measurements themselves. The thermocouples were 0.13 mm in diameter. Three thermocouples were inserted into one cell in the axial direction, and another three were inserted into the second cell along the radial direction. In addition, six thermocouples were placed on the can wall of each cell.

6. Results and discussion

6.1. Comparisons between simulated results and measured results

Fig. 12 shows comparisons between the time evolutions of temperatures of the 18650-type lithium-ion cell obtained via experiment and those calculated by the two-way coupled
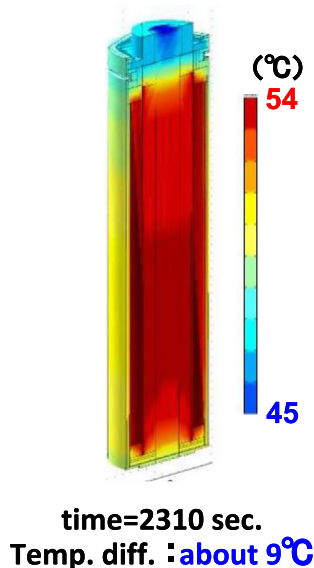

Fig. 17. Simulated temperature distribution inside the cell at the end of charge–discharge cycle. Applied current is 5 A (10C), and ambient temperature is 20 °C.

simulation method. The lower two sawtooth lines compare time variations of cell potential. Applied current is 2.5 A (5C). The ambient temperature and the initial temperature of the prepared cell were set at 0 °C. It should be noted that the temperatures in this figure reflect the average value of the measured temperatures because differences at each measured point were within one degree, as shown in Fig. 13. However, the maximum temperature difference across the entire cell was about five degrees because of the large heat mass at the upper side. It is noteworthy that the time variations of temperature measurements, both inside the cell and on the can wall, were simulated within three degrees of accuracy, and that the simulation of the temperature fluctuation during the charge–discharge cycle could be performed with high accuracy.

Other validation calculation results are exhibited in the following figures. Fig. 14 shows the results in a case where the applied current is 2.5 A (5C) and ambient temperature is 20 °C. From Fig. 15, it can be seen that the maximum temperature difference across the entire cell becomes about four degrees at the end of the charge–discharge cycle in this case. Additionally, Fig. 16 shows the result of a case where the applied current is 5 A (10C) and ambient temperature is 20 °C, in which case the maximum temperature difference across the entire cell reaches about nine degrees, as shown in Fig. 17.

Based on these validation results, it can be seen that the two-way electrochemical-thermal coupled simulation method presented in this paper is capable of simulating temperatures inside the cell and on the can wall with an accuracy level within a few degrees.

6.2. Contribution of each heat release source term

In this section, we will devote a little more space to discussing the contribution of each heat source term to total electrochemical heat release rate.

As previously mentioned, the local electrochemical heat release rate consists of three heat source terms that are expressed in Eq. (1) and/or Eq. (60):

$$Q_{\text{elchem}} = Q_{\text{ohmic}} + Q_{\text{irrev}} + Q_{\text{rev}} \tag{66}$$

The first term on the right-hand side refers to the ohmic heat caused by ionic resistance. The second term represents the irreversible heat arising from overpotential and film resistance. The third term expresses the reversible heat resulting from the entropic effect of lithium intercalation or deintercalation. These three terms are formulated as follows:

$$Q_{\text{ohmic}} = \sum_{j=n,\,p} \left(\sigma_j^{\text{eff}} \nabla \phi_{s,\,j} \cdot \nabla \phi_{s,\,j} \right) + \sum_{j=n,\,\text{sep},\,p} \left(\kappa_j^{\text{eff}} \nabla \phi_{e,\,j} \cdot \nabla \phi_{e,\,j} \right. \\ \left. + \kappa_{D,\,j}^{\text{eff}} \nabla \ln c_{e,\,j} \cdot \nabla \phi_{e,\,j} \right) \tag{67}$$

$$Q_{\text{irrev}} = \sum_{j=n,\,p} a_{s,\,j} \bar{i}_{n,\,j} \left(\overline{\phi}_{s,\,j} - \overline{\phi}_{e,\,j} - U_j \right) \tag{68}$$

$$Q_{\text{rev}} = \sum_{j=n,\,p} a_{s,\,j} \bar{i}_{n,\,j} T \frac{\partial U_j}{\partial T} \tag{69}$$

Fig. 18 displays the effect of each three heat source term on time variations of temperature of the cell during the charge–discharge cycle at the 5C rate (2.5 A), 0 °C. Here, only one-cycle discharge–charge process is shown. As indicated in Fig. 18(a), a small temperature fluctuation is observed inside the cell. Fig. 18(b) and (c)
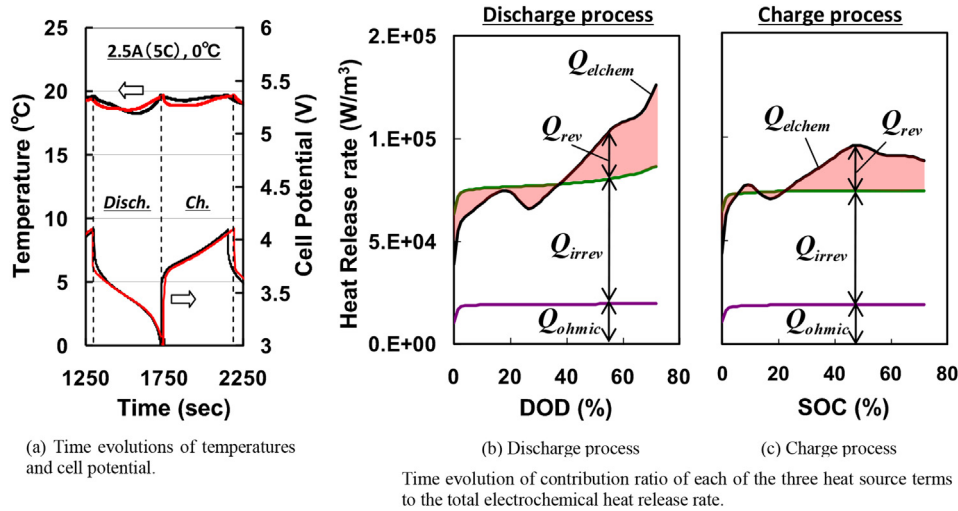
(a) Time evolutions of temperatures and cell potential.

(b) Discharge process

(c) Charge process

Time evolution of contribution ratio of each of the three heat source terms to the total electrochemical heat release rate.

Fig. 18. Effect of each heat source term on time variations of temperature of the cell during the charge−discharge cycle at the 5C rate (2.5 A), 0 °C. The small fluctuation of the temperature behavior is mainly caused by the reversible heat resulting from entropic effect due to lithium-ion intercalation or deintercalation.
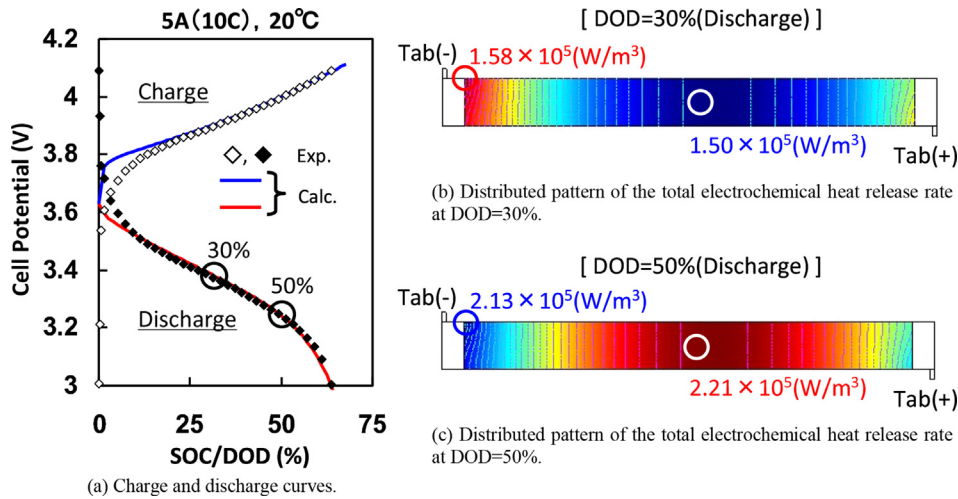

(a) Charge and discharge curves.

(b) Distributed pattern of the total electrochemical heat release rate at DOD=30%.

(c) Distributed pattern of the total electrochemical heat release rate at DOD=50%.

Fig. 19. Time evolutions of distributed patterns of the total electrochemical heat release rate across the entire electrode plane during discharge process at the 10C rate (5 A), 20 °C.

shows the time variations of the contribution ratio for each of the three heat source terms in relation to the total electrochemical heat release rate during the discharge and charge process, respectively. From these figures, it is clear that the ohmic heat is similar in value between discharge and charge and remains constant over the entire process. In addition, it can be seen that the irreversible heat is also similar in value between both processes and maintains nearly constant. As a result, a remarkable difference is observed in the reversible heat, which is expressed by Eq. (69).

The time variation of the total electrochemical heat release rate is directly reflected in the thermal behavior of the cell, as shown in Fig. 18. Furthermore, the reversible heat governs the time variation behavior of the heat generation rate. Accordingly, these results lead to the conclusion that the small fluctuation noted in the temperature behavior is caused primarily by the reversible heat.

Reversible heat variations depend on the local state of charge (SOC) of the anode and cathode active materials during the discharge and charge process. In order to evaluate the reversible heat, the entropy change ΔS value of the active materials, which is related to the derivative of the open circuit potential (OCP) with respect to temperature, is necessary. In this study, instead of measuring ΔS directly, we used a model formulation that predicts

the entropy change based on experimental data of the OCP. Details of the model used for entropy change are provided in Appendix B.

6.3. Distribution of heat generation rate

In the two-way coupled simulation method presented in this paper, the electrochemical phenomena of lithium-ion batteries are simulated using the quasi-3D porous electrode solver. Hence, the 2D distributed information of a heat generation rate arising from electrochemical reactions across an entire electrode plane can be obtained.

Fig. 19 shows the distribution of a heat generation rate across an entire unrolled electrode plane. Fig. 19(a) shows comparisons between charge and discharge curves obtained from experiments and simulated results at the 10C rate (5 A), 20 °C, while Fig. 19(b) and (c) shows distributed patterns of the total electrochemical heat generation rate when the DOD in the discharge process equals 30% and 50%, respectively.

At DOD = 30%, the maximum heat generation rate puts in an appearance at the end near the negative tab, while the minimum value occurs at the central region. In contrast, the distributed pattern of the heat generation rate turns around at DOD = 50%. In

other words, the distributed pattern of the total electrochemical heat generation rate varies moment by moment depending on the DOD or SOC.

From these figures, it can be seen that the range between maxima and minima of the total electrochemical heat generation rate across the entire electrode plane reaches 5% at the 10C rate discharge in the case of 18650-type cell of 0.5 Ah. As for the 5C rate discharge, it reaches the vicinity of 1%; however, the figure showing the calculation results is omitted here. Accordingly, it is easy to imagine that the ununiformity of the total heat generation rate across the entire electrode plane becomes larger as the applied current rate increases.

7. Conclusions

An enhanced single particle (ESP) charge–discharge model for lithium-ion batteries has been developed. This ESP model handles each negative and positive electrode as a single spherical particle in the electrolyte phase. The potential and lithium-ion concentration in the electrolyte phase are set at the representative position in each electrode, and the distributions of these physical properties across the thickness of the electrode are approximated by parabolic profiles. The use of these model features facilitate more accurate calculations of the charge–discharge curve under high rate conditions than are possible using the conventional SP model because the potential drop in the electrolyte phase can be simulated in the new model.

This ESP model is inexpensive in terms of cost and computation time requirements because it uses the mass-point system. In addition, because the accurate estimation of the heat generation rate requires information on potential and lithium-ion concentration in the solution phase, the ESP model is capable of estimating the heat generation rate caused by electrochemical reactions more accurately than previous methods.

The above two advantages have contributed significantly to the development of our multi-dimensional two-way electrochemical-thermal coupled simulation method. This method has been applied to a thermal behavior analysis of the charge–discharge cycle of an 18650-type lithium-ion cell battery, where good agreement between the simulation and actual measurements was achieved. Furthermore, the results clearly show that the small temperature behavior fluctuation observed during the charge–discharge cycle is caused primarily by the reversible heat resulting from the entropic effect arising from lithium intercalation or deintercalation.

Appendix A. Cell thermal solver and coordinate transformation for data mapping between electrode and cell thermal models

In the thermal analysis of a battery cell interior, supposing the convective velocities of gas enclosed in a cell and an electrolyte are minute and can be ignored, the governing equation of a thermal field turns into the following 3D heat conduction equation.

$$\rho C_p \frac{\partial T}{\partial t} = \nabla(\lambda \nabla T) + q \tag{A1}$$

Here, ρ, C_p and λ are density, specific heat and thermal conductivity, respectively.

A normal battery cell consists of a top cap, packing, a collector tab, an insulator, a spacer (gas), etc., in addition to the electrode and the can. The thermo physical properties value (density, specific heat, thermal conductivity) of each of those constructional elements is provided for in the simulation. However, although a wound electrode is in a state where the anode, the cathode, and separator are impregnated with the electrolyte, the space between the positive and negative electrodes is narrow and temperature differences are small. Furthermore, since it is difficult to treat them individually when considering the spatial resolution of 3D thermal analysis, an electrode is treated as a single unit. At that time, the average physical properties value was given as follows.

First, the individual thermo physical properties values of the electrolyte, anode, cathode, and separator are specified. In the pores of the positive/negative electrodes and separator, which are filled with electrolyte, the value of each physical property is estimated as a volume average of the solid and liquid phases using their percentage of the void. Finally, the average physical properties value of a laminated electrode is computed. The density and specific heat are estimated as a weight-average of the thickness of each part for electrode laminated structure. On the other hand, while the thermal conductivity of a radial (electrode thickness) direction differs from those of the other two directions (a circumference, an axis), they are given by the following formulas for all directions.

$$\lambda_{t,z} = \frac{\sum_i \lambda_i \delta_i}{\sum_i \delta_i}, \quad \lambda_r = \frac{\sum_i \delta_i}{\sum_i \frac{\delta_i}{\lambda_i}} \tag{A2}$$

Here, the subscripts t, z and r refer to the circumferential, axis and radial directions in the cylindrical coordinates system based on the central axis of a spirally wound object. Additionally, δ is thickness, and the subscript i shows the lamination component of electrode for one cycle.

Next, the coordinate transformation for data mapping between a 2D electrode plane mesh and a 3D spirally wound thermal model mesh is described. Here, the relationship between the x-coordinate of the 2D electrode deployment direction and the radius r and an angle θ of a spirally wound object are as follows:

$$r = r_0 + \frac{a}{2\pi}\theta \tag{A3}$$

$$\theta = \sqrt{\left(\frac{2\pi r_0}{a}\right)^2 + \frac{4\pi x}{a}} - \frac{2\pi r_0}{a} \tag{A4}$$

Here, r_0 is the inner end radius and a is a pitch of one cycle of electrode lamination as shown in Fig. 20. It should be noted that θ [rad] is not 2π cycle but monotonically increases with the number of windings.

Appendix B. Model for entropy change during intercalation and deintercalation

In this Appendix, we describe the model used to predict the entropy change necessary for estimating the reversible heat (see Section 6.2). The entropy change due to intercalation and deintercalation is experimentally obtained by measuring the
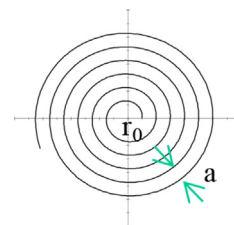

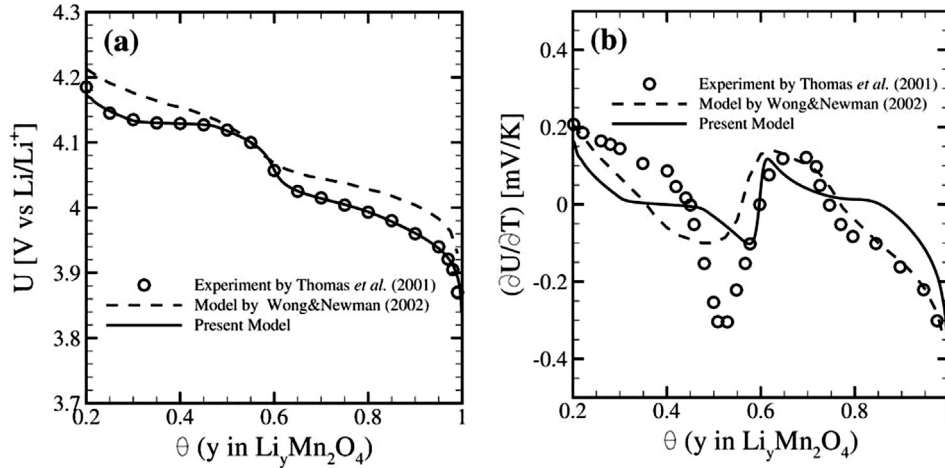**Fig. 20.** Illustration of a spirally wound object.

Fig. 21. Comparison of the model prediction and experimental results. (a) Open circuit potential U. (b) Entropy change ($\partial U/\partial T$) = $\Delta S/F$. The solid line indicates the present results, the dashed line indicates the model prediction by Wong and Newman [29], and the symbol indicates the experimental results provided by Thomas et al. [28].

temperature dependence of the open circuit potential (OCP). However, performing this measurement is difficult because it takes a significant amount of time to reach the equilibrium state (at which the OCP can be measured) after the temperature is changed. In contrast, the model described in this Appendix predicts the temperature dependence based solely on the OCP data at a fixed temperature.

The model is premised on the assumption that the active material consists of N independent components that have different reaction properties. This is a model for describing the stepwise change of the OCP depending on the SOC, which is used by Zhang et al. [26] to derive a kinetic model.

We begin by introducing several variables into the model description. Let θ be the ratio of the number of intercalated lithium atoms to the total number of the sites in the active material. In addition, let Θ_k and θ_k denote the ratios of the number of the sites, and the number of lithium atoms in kth component, respectively, to the total number of sites in the active material:

$$\sum_{k=1}^{N} \Theta_k = 1, \quad \sum_{k=1}^{N} \theta_k = 0. \tag{B1}$$

Following the discussion in Ref. [26], starting from the Butler–Volmer kinetics for multi-component material, the following relation, which holds at the equilibrium state, is derived:

$$U = U_k^0 + \frac{RT}{F} \ln\left(\frac{\Theta_k - \theta_k}{\theta_k}\right)^{\xi_k}, \tag{B2}$$

where U_k^0 is a quantity related to the reaction rate, and ξ_k is the order of the reaction of the kth component. Solving Eq. (B2) with respect to θ_k and substituting into Eq. (B1) yields

$$\theta = \sum_{k=1}^{N} \frac{\Theta_k}{1 + \exp\left(\frac{F}{\xi_j RT}\left(U - U_k^0\right)\right)}. \tag{B3}$$

This relationship between θ and U with the model parameters Θ_k, U_k^0, and ξ_k coincides with the OCP model proposed semi-empirically by Verbrugge and Koch in their work on modeling graphite electrodes [27]. Differentiation of Eq. (B3) with respect to T gives the quantity related to the entropy change ΔS through ($\partial U/\partial T$) = $\Delta S/F$:

$$T\left(\frac{\partial U}{\partial T}\right) = \frac{\sum_{k=1}^{N} \frac{\Theta_k E_k}{\xi_k (1+E_j)^2}\left(U - U_k^0\right)}{\sum_{k=1}^{N} \frac{\Theta_k E_k}{\xi_k (1+E_j)^2}}, \tag{B4}$$

where

$$E_k = \exp\left(\frac{F}{\xi_k RT}\left(U - U_k^0\right)\right). \tag{B5}$$

Once we have the (B3) relationship fitted to a θ–U curve measured experimentally, the predicted values of entropy change are drawn immediately using the same set of model parameters Θ_k, U_k^0, and ξ_k. Note that the coefficient U_k^0, which is related to the reaction rate, is intrinsically a function of temperature. In the above derivation, however, we ignore the dependency of U_k^0 on temperature in view of the fact that the dependency vanishes in cases where the frequency factor value is common to the anodic and cathodic reaction.

The adequacy of the model is assessed by comparison with the experimental results by Thomas et al. [28] They measured the OCP and $\partial U/\partial T$ of lithium manganese spinel (Li$_y$Mn$_2$O$_4$) at various values of θ. The values of the model parameters Θ_k, U_k^0, and ξ_k were determined by fitting Eq. (B3) with $N = 6$ to the experimental data of the OCP. The method we employed to accomplish this is the standard nonlinear general reduced gradient (GRG) optimization algorithm. We then estimated the values of $\partial U/\partial T$ using Eq. (B4). Fig. 21 compares the results of the present model and Ref. 27. Although the present model underestimates the value of ($\partial U/\partial T$) = $\Delta S/F$ in the intermediate region of θ, the overall entropy change trend is captured well. In the figure, the results of the model provided by Wong and Newman [29] are also shown. In their model, both the OCP and $\partial U/\partial T$ are predicted. The accuracy of the entropy change is almost the same as the present model, whereas the reproduction of the OCP of the present model is more accurate.

List of symbols

a_s	specific interfacial area of an electrode (m² m⁻³)
c_e	Li⁺ concentration in the electrolyte phase (mol m⁻³)
c_s	Li concentration in the solid particles (mol m⁻³)
c_{se}	Li concentration at the surface of the solid particles (mol m⁻³)

D_e	diffusion coefficient of Li$^+$ in the electrolyte phase (m^2 s^{-1})
D_s	diffusion coefficient of Li$^+$ in the solid phase (m^2 s^{-1})
F	Faraday's constant (96,487C mol^{-1})
I_{app}	applied current density (A m^{-2})
i_0	exchange current density (A m^{-2})
$\overline{i_n}$	superficial current density (A m^{-2})
j	local volumetric transfer current density due to charge transfer (A m^{-3})
l_{se}	diffusion length of Li$^+$ from solid−electrolyte interface into solid phase (m)
L	thickness of n, sep or p (m)
q	heat generation rate (W m^{-3})
R	universal gas constant (8.3143 J/(mol^{-1}·K))
R_f	film resistance on an electrode surface (Ω m^2)
r	radial coordinate (m)
r_s	radius of the spherical particles (m)
T	absolute temperature (K)
t	time (s)
t_+°	transference number of Li$^+$ in solution
U	open-circuit potential of an electrode reaction (V)
x, y	coordinates on the unrolled electrode plane (m)
z	coordinate across the thickness of the electrode (m)

Greek symbols

α_a, α_c	anodic and cathodic transfer coefficients for an electrode reaction
ε	volume fraction of a phase
η	surface overpotential of an electrode reaction (V)
κ	conductivity of the electrolyte (S m^{-1})
κ_D	diffusional conductivity of the electrolyte (A m^{-1})
σ	conductivity of the electrode (S m^{-1})
ϕ_s	electrical potential in the solid phase (V)
ϕ_e	electrical potential in the electrolyte phase (V)

Subscript and superscript

eff	effective

j	n or p
Li	lithium species
n	negative electrode
p	positive electrode
sep	separator

References

[1] W.B. Gu, C.Y. Wang, Lithium Batteries, PV 99-25, in: The Electrochemical Society Proceedings, 1999, pp. 748−762.
[2] W.B. Gu, C.Y. Wang, J. Electrochem. Soc. 147 (2000) 2910−2922.
[3] L. Rao, J. Newman, J. Electrochem. Soc. 144 (1997) 2697−2704.
[4] P.M. Gomadam, J.W. Weidner, R.A. Dougal, R.E. White, J. Power Sources 110 (2002) 267−284.
[5] C.R. Pals, J. Newman, J. Electrochem. Soc. 142 (1995) 3274−3281.
[6] C.R. Pals, J. Newman, J. Electrochem. Soc. 142 (1995) 3282−3288.
[7] Y. Chen, J.W. Evans, J. Electrochem. Soc. 140 (1993) 1833−1838.
[8] Y. Chen, J.W. Evans, J. Electrochem. Soc. 141 (1994) 2947−2955.
[9] Y. Chen, J.W. Evans, J. Electrochem. Soc. 143 (1996) 2708−2712.
[10] U.S. Kim, C.B. Shin, C.S. Kim, J. Power Sources 180 (2008) 909−916.
[11] U.S. Kim, C.B. Shin, C.S. Kim, J. Power Sources 189 (2009) 841−846.
[12] R. Spotnitz, J. Franklin, J. Power Sources 113 (2003) 81−100.
[13] G.H. Kim, A. Pesaran, R. Spotnitz, J. Power Sources 170 (2007) 476−489.
[14] M. Doyle, T.F. Fuller, J. Newman, J. Electrochem. Soc. 140 (1993) 1526−1533.
[15] D. Bernardi, E. Pawlikowski, J. Newman, J. Electrochem. Soc. 132 (1985) 5−12.
[16] B.S. Haran, B.N. Popov, R.E. White, J. Power Sources 75 (1998) 56−63.
[17] V.R. Subramanian, J.A. Ritter, R.E. White, J. Electrochem. Soc. 148 (2001) E444−E449.
[18] G. Ning, B.N. Popov, J. Electrochem. Soc. 151 (2004) A1584−A1591.
[19] S. Santhanagopalan, Q. Guo, P. Ramadass, R.E. White, J. Power Sources 156 (2006) 620−628.
[20] Q. Zhang, R.E. White, J. Power Sources 165 (2007) 880−886.
[21] Q. Zhang, R.E. White, J. Power Sources 179 (2008) 793−798.
[22] C.Y. Wang, W.B. Gu, B.Y. Liaw, J. Electrochem. Soc. 145 (1998) 3407−3417.
[23] M. Doyle, J. Newman, A.S. Gozdz, C.N. Schmutz, J.-M. Tarascon, J. Electrochem. Soc. 143 (1996) 1890−1903.
[24] C.Y. Wang, V. Srinivasan, J. Power Sources 110 (2002) 364−376.
[25] AVL FIRE® Version, 2009. Manual.
[26] Q. Zhang, Q. Guo, R.E. White, J. Electrochem. Soc. 153 (2006) A301−A309.
[27] M.W. Verbrugge, B.J. Koch, J. Electrochem. Soc. 150 (2003) A374−A384.
[28] K.E. Thomas, C. Bogatu, J. Newman, J. Electrochem. Soc. 148 (2001) A570−A575.
[29] W.C. Wong, J. Newman, J. Electrochem. Soc. 149 (2002) A493−A498.